Materials Science & Engineering A 878 (2023) 145233

Contents lists available at ScienceDirect

Materials Science & Engineering A

journal homepage: www.elsevier.com/locate/msea

Evolution of microstructure and mechanical properties in gas tungsten arc welded dual-phase $Fe_{50}Mn_{30}Co_{10}Cr_{10}$ high entropy alloy

J.G. Lopes [a], Priyanka Agrawal [b,c], Jiajia Shen [a,e], N. Schell [d], Rajiv S. Mishra [b,c], J.P. Oliveira [a,e,*]

[a] UNIDEMI, Department of Mechanical and Industrial Engineering, NOVA School of Science and Technology, Universidade NOVA de Lisboa, Caparica, 2829-516, Portugal
[b] Center for Friction Stir Processing, Department of Materials Science and Engineering, University of North Texas, Denton, TX, 76207, USA
[c] Advanced Materials and Manufacturing Processes Institute, University of North Texas, Denton, TX, 76207, USA
[d] Institute of Materials Physics, Helmholtz-Zentrum Hereon, Max-Planck-Str. 1, Geesthacht, D21502, Germany
[e] CENIMAT/I3N, Department of Materials Science, NOVA School of Science and Technology, Universidade NOVA de Lisboa, 2829-516, Caparica, Portugal

ARTICLE INFO

Keywords:
High entropy alloys
Gas tungsten arc welding
Synchrotron X-ray diffraction
Microstructure
Mechanical testing
Thermodynamic simulations

ABSTRACT

In recent years, high entropy alloys (HEAs) have been shown to be promising alternatives to common engineering alloys, depending on their composition and thermomechanical processing. Up to now, several works aimed at improving the mechanical properties and discovering different HEAs given the extremely large compositional possibilities made available by the multicomponent approach associated to these materials. Their processability, however, is an important topic that must be studied. Welding is a key manufacturing technique that will eventually be applied to HEAs. Thus, there is a need to evaluate the microstructure and property changes induced by the weld thermal cycles, to assess the suitability of certain welding process/HEAs combinations for possible industrial applications. In the present work, Gas Tungsten Arc Welding (GTAW) was used to achieve defect-free joints based on a novel transformation induced plasticity (TRIP) $Fe_{50}Mn_{30}Co_{10}Cr_{10}$ HEA. The microstructure and mechanical behavior of the joints were assessed by means of optical and electron microscopy, synchrotron X-ray diffraction, thermodynamical calculations, microhardness mapping and tensile testing. Overall, an excellent mechanical performance was obtained on the resulting joints, opening the door for their adoption in real-life applications.

1. Introduction

Since 2004, with the independent seminal works of Cantor and Yeh [1,2], high entropy alloys (HEAs) have been subject to extensive research, either to formulate new compositions [3–6] or to assess their applicability for meaningful purposes [6–9].

From the multiple combinations that already have been discovered since the inception of HEAs, the $Fe_{50}Mn_{30}Co_{10}Cr_{10}$ alloy has interesting features that make it a competitive choice for a wide range of applications. Although exhibiting some similarity in composition with the Cantor alloy (equiatomic FeMnCoCrNi), the absence of Ni makes it a less expensive and interesting alternative. Additionally, the transformation induced plasticity (TRIP) effect exhibited by this HEA once mechanically deformed, effectively transforms the face centered cubic phase (γ-FCC) parent phase into the metastable hexagonal closed packed (ε-HCP) phase via a martensitic transformation, granting this HEA a dual-phase (DP) constitution, which is the reason why, from this point on, it will be referred to as DP-HEA [10]. The TRIP deformation mechanism, coupled with dislocation slip, can provide this DP-HEA an excellent strength-ductility synergy.

Such phase metastability combined with the concepts of high entropy alloy design is a systematic topic in the current literature [11–15], which can yield several different options for the improvement of the deformation behavior on a material, making it a potential alternative to conventional alloys. More specifically, in the case of the DP-HEA, the TRIP deformation mechanism coupled with dislocation slip, can provide this DP-HEA an excellent strength-ductility synergy.

Nevertheless, to prevent premature failure when in service, the processability of any alloy must be thoroughly analyzed once a promising material composition has been determined. For such, as a crucial aspect of the manufacturing process, one must combine the metallurgical and mechanical characteristics of the material with the possible

* Corresponding author. CENIMAT|i3N, Department of Materials Science, School of Science and Technology, NOVA University Lisbon, Caparica, Portugal.
E-mail address: jp.oliveira@fct.unl.pt (J.P. Oliveira).

https://doi.org/10.1016/j.msea.2023.145233
Received 13 April 2023; Received in revised form 23 May 2023; Accepted 2 June 2023
Available online 3 June 2023

manufacturing routes to which the material might be subjected prior to its deployment for a specific application.

Welding is a well-established set of processes that can generate strong and permanent bonds between multiple components and is often used on the development of products for both functional and structural applications [16]. Furthermore, welding often results on local microstructural variations of the processed material which, in turn, can alter the mechanical behavior of such parts. Among the many welding processes that exist, Gas Tungsten Arc Welding (GTAW) is a relatively easy to handle and low-cost process that is widely available industrially [17]. Nevertheless, although some studies on the processability and behavior of DP-HEA have already been published [18–25], the current literature lacks a specific metallurgical and mechanical analysis on the processability of this HEA, especially regarding welding, to the best of the authors knowledge.

As such, in this paper, GTAW was performed on the $Fe_{50}Mn_{30}Co_{10}Cr_{10}$ DP-HEA. Multiple characterization techniques were employed to study the varying microstructural features across the welded joint. These techniques encompassed optical microscopy, electron backscattered imaging and synchrotron x-ray diffraction to study role of the thermal cycle on the microstructure developed at different distances to the heat source. Mechanical performance of the joint was also assessed by means of microhardness mapping and tensile testing coupled with digital image correlation. The present work aims at offering a welding-standpoint analysis for DP-HEA, while shedding light on its the processing-microstructure-properties relationships.

2. Materials and methods

Prior to welding, 30 × 30 × 1.5 mm plates were cut from an as-cast $Fe_{50}Mn_{30}Co_{10}Cr_{10}$ (at. %) DP-HEA ingot, with a precision cutting machine. After cleaning with acetone to remove any residue from the cutting process, the samples were welded by GTAW. Samples were welded with direct current and straight polarity with a TELWIN Technology TIG 182 AC/DC-HF/LIFT welding machine, using a 2.4 mm Tungsten electrode 2% Lanthanated. The parameters utilized included an intensity of 25 A and a torch travelling speed of 200 mm/min. While the torch was kept at a distance of 1.5 mm from the sample, 99.999% pure Argon shielding gas was applied on the face (flow rate of 8 l/min) and the root (flow rate of 5 l/min) to prevent material oxidation and/or contamination from the surrounding atmosphere. After welding, electric discharge machining was utilized to obtain tensile specimens for further characterization, with dimensions as displayed in Fig. 1.

For microstructural analysis, the welded samples were mechanically polished and etched with a 2% Nital solution. Scanning electron microscopy (SEM) using a Hitachi SU8000, was used to probe the as-welded microstructure and the surface fractures of the joints after tensile testing. Energy dispersive X-ray spectroscopy (EDS) and electron backscattered diffraction (EBSD) measurements were performed in a FEI Nova NanoSEM 230 with EDAX Hikari Super EBSD equipment. Analysis of the EBSD data was performed using TSL OIM Analysis 7.2 and Image J software and analysis of grain size was conducted using the linear intercept method, considering at least 10 grains in each region.

Synchrotron X-ray diffraction, on the full extension of the weld was done at the P07B beamline at PETRAIII/DESY. The experimental setup allowed to perform the scans in transmission mode, providing insightful information on the microstructure evolution across the welded joints. The experiments were performed at a sample to detector distance of 1.235 m, with an energy of 87.1 keV (corresponding to a wavelength of 0.14235 Å) and a beam size of 200 × 200 μm, with a 200 μm incremental steps between consecutive analyzed points. The obtained Debbye-Scherrer rings were fully integrated along the azimuthal using pyFAI [26] and further analysis was performed with the aid of in-house developed python-based scripts, by means of fitting the synchrotron data with a Voigt profile.

Using ThermoCalc software, thermodynamic calculations using the Scheil-Gulliver module were performed to predict the phases that may form during the fast cooling and non-equilibrium solidification conditions of the molten pool, as typical during arc-based welding processes. For these thermodynamic calculations the TCHEA5 database was used. Comparison of the thermodynamically predicted microstructure and the experimentally determined one provides a way to further validate the thermodynamic databases for HEAs.

For mechanical property analysis, microhardness mapping was performed on the weld cross joint using a Mitutoyo Micro Hardness Testing Machine HM-112. A 500 g load, kept during 10 s, was utilized and a 150 μm distance was maintained between consecutive indentations. Additionally, tensile testing of the samples was performed with the tensile load being applied perpendicularly to the welding direction. The joints tensile properties were benchmarked against the as-cast base material. Tensile testing was performed using an Autograph Shimadzu AG50kNG machine, equipped with a 50 kN load cell at a 0.02 mm/s testing speed. Digital Image Correlation (DIC) was employed to assess the load partitioning undertaken by each of the welded regions.

3. Results and discussion

3.1. Microstructural analysis

Upon visual inspection of the joints cross section, autogenous $Fe_{50}Mn_{30}Co_{10}Cr_{10}$ DP-HEA welds with full penetration were obtained, as shown in Fig. 2 (a). Also in Fig. 2 (a), it is possible to observe the effect of the thermal cycle across the microstructure of the welded joint. The base material (BM), heat affected zone (HAZ) and fusion zone (FZ) are delimitated to further help in establishing differences in microstructure at each location within the joint.

Focus is now given to representative locations within the welded joint as observed by light optical microscopy. Analysis of the BM details the initial condition of the material prior to welding. As it can be observed in Fig. 2 (b), the material is composed by two phases: austenite (γ-FCC), characterized by equiaxed grains with an average size of 27.2 ± 10.7 μm, and ε-martensite (ε-HCP) which corresponds to the needle-

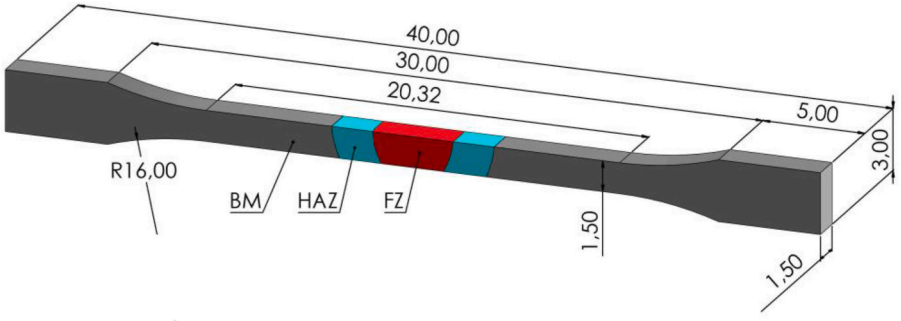

Fig. 1. Geometry and dimensions of tensile specimens. BM – base material; HAZ – heat affected zone; FZ – fusion zone (all dimensions in mm).

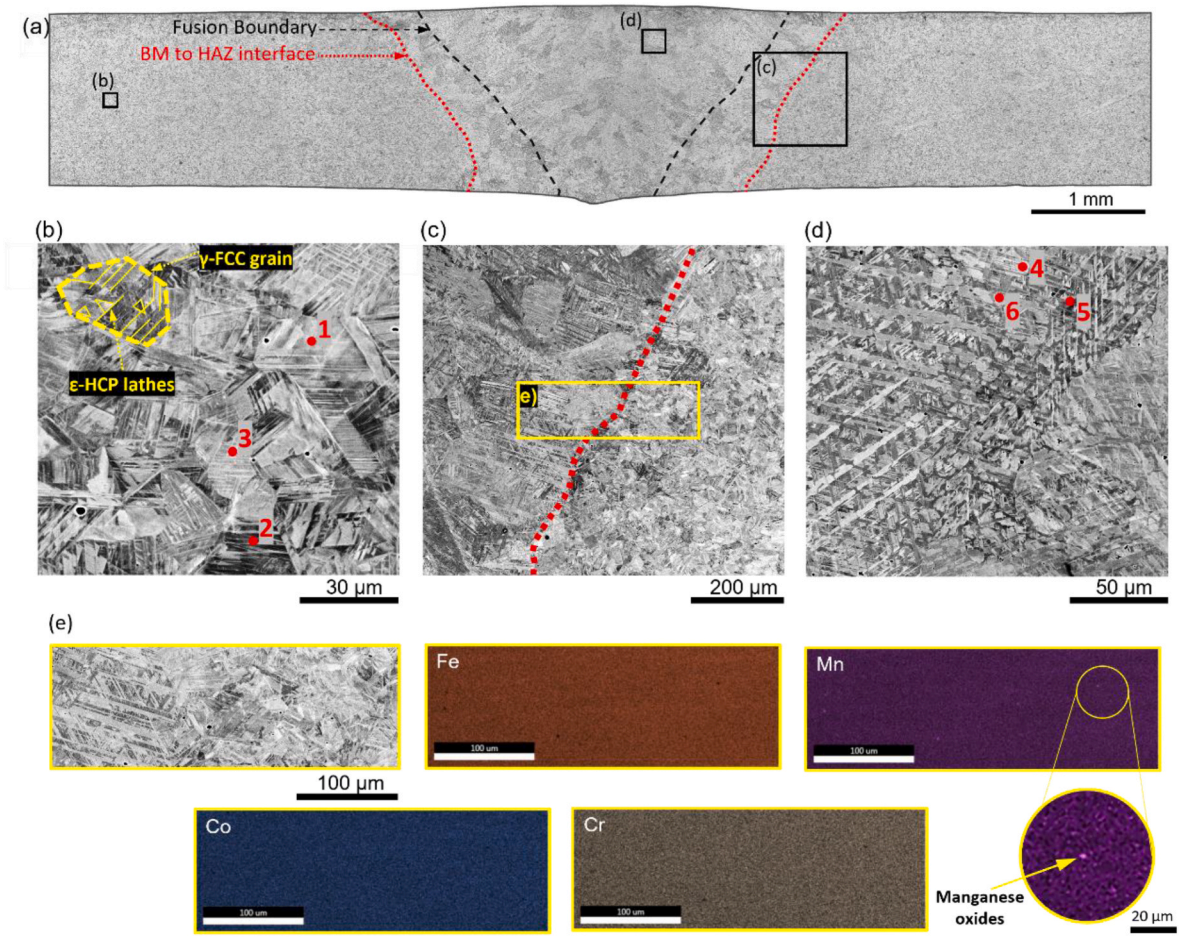

Fig. 2. Microstructure of the $Fe_{50}Mn_{30}Co_{10}Cr_{10}$ HEA welded joint: (a) Macrograph detailing the joint cross section, indicating the BM to HAZ interface and the fusion boundary; (b) BM, where a parent γ-FCC grain is highlighted with a yellow dashed line, while the ε-HCP laths are also shown; (c) BM to HAZ interface; (d) FZ; (e) EDS mapping of the BM to HAZ interface. The red dots in b) and d) detail locations where EDS point analysis was performed. The yellow box c) details the location for EDS mapping. (For interpretation of the references to color in this figure legend, the reader is referred to the Web version of this article.)

shaped laths within the grains. In the case of this TRIP DP-HEA, the presence of martensitic laths in the as-cast condition can be explained by the phase transformation arising from the internal strains developed during solidification and contraction of the material as it cools down from casting, causing the lattice atoms to rearrange in a different crystal structure from the parent FCC phase [27].

Adjacent to the BM exists the HAZ. Fig. 2 (c) portraits the transition from the BM to the HAZ clearly exhibiting a grain size variation upon entering in the latter region. The temperature and permanence time at temperatures where solid-state transformations can arise enabling for grain growth to occur leading to a significantly larger grain size of 112.2 ± 14.8 μm. That is, as the welding heat flowed through conduction from the FZ towards the solid material, there will be recrystallization phenomena, but eventually grain growth will be predominant. It should be noted, however, that favoring of a grain growth mechanism over recrystallization is not only dependent on the welding parameters but also on the distance to the heat source: regions of the HAZ further away for the heat source, i.e., that experience lower peak temperatures, will be dominated by recrystallization phenomena, while for those closer to the fusion boundary grain growth will be predominant.

To assess and compare the potential existence of compositional changes between the BM and FZ, EDS point analysis was performed considering three points in each region. These results are summarized in Table 1, showing that the composition is practically constant along the analyzed points, although slightly different from the nominal composition of the present DP-HEA: $Fe_{50}Mn_{30}Co_{10}Cr_{10}$. Overall, the EDS point measurements performed are close to the alloy nominal composition, with the minor changes observed being related to the casting of the alloy, as well as to the semi-quantitative nature of SEM/EDS measurements.

Table 1
Compositional measurements, as obtained by point EDS, in the BM and the FZ.

Region	Point	Atomic percentage [%]			
		Fe	Mn	Co	Cr
BM	**1**	50.4	29.2	11.2	9.2
	2	51.4	28.2	11.1	9.3
	3	50.4	29.2	11.4	9.0
FZ	**4**	53.1	26.8	11.0	9.1
	5	45.9	33.5	11.5	9.2
	6	53.3	23.7	10.9	9.2

EDS mapping in a region comprising both the BM and HAZ was also performed, as shown Fig. 2 (e). A homogenous composition distribution is observed. However, sparsely dispersed Mn-rich oxides are observed. These can be assigned to Mn oxides, as previously found in [28].

Delving into the FZ, refer to Fig. 2 (a), it is possible to observe large and elongated grains with an average γ-FCC grain size of 124.2 ± 16.4 μm, aligned towards the weld center line. This occurs due to the overall tendency for grains to grow epitaxially from the pre-existing BM in the opposite direction of the heat flow during solidification of the melt pool. On closer analysis, dendrites and martensitic laths, the latter being

formed as a stress relieving mechanism or through stacking faults to cope with the internal stresses developed upon cooling [27], can be observed within the grains, as shown in Fig. 2 (d).

A large-scale EBSD map was performed to further evaluate changes in both grain size and orientation along the welded joint, as depicted in Fig. 3 (a). The corresponding phase map is shown in Fig. 3 (b). Considering the inverse pole figure (IPF) data of Fig. 3 (a), is possible to observe the previously referred epitaxial growth at the HAZ/FZ interface (delimited by the black dashed lines), while toward the center of the FZ competitive grain growth is predominant. Upon heat extraction from the melt pool to the colder HAZ and BM, grains start to grow in the opposite direction and those who have the preferred growth direction aligned with the maximum heat extraction direction, typically perpendicular to the HAZ/FZ boundary, will have their growth facilitated at the expense of poorly oriented and newly formed grains. While near the weld centerline grains are approximately equiaxed, despite being coarse, outside of this region the grains are predominantly columnar and grew perpendicularly to the HAZ/FZ boundary. This is also related to changes in the thermal and solidification conditions, namely thermal gradient, G, and growth rate, R, that are known to modify the grain morphology during material solidification.

In the EBSD phase map of Fig. 3 (b) is observed that the microstructure along the joint is composed of both γ-FCC from the ε-HCP phases, in good agreement with that was previously observed by light optical microscopy. Comparing the BM and FZ regions reveals that in the latter the γ-FCC phase is predominant over the ε-HCP phase. In contrast, in the BM, the ratio of both phases' approaches unity. For comparison, the evolution of phase fractions obtained in each region (BM, HAZ and FZ), calculated using ImageJ, is detailed in Table 2.

As it is possible to perceive, going from the BM to the HAZ, that the ε-HCP phase fraction increases by 13%, while transitioning from the HAZ to the FZ is clear that the γ-FCC phase fraction is superior to that measured in the other regions, reaching 71.1%. The phase distribution that characterizes this welded joint depends on the different processing conditions that the BM (in the as-cast condition) and the FZ were subjected during welding, which eventually was responsible for generating the ε-HCP phase. In the HAZ, the higher phase fraction of ε-HCP can be explained by the initial condition of the BM, which already contains ε-HCP laths that act as nucleus for the continuous transformation of γ-FCC into ε-HCP. This transformation occurs as the temperature rapidly decreases due to the heat sink effect of the BM and of the shielding gas, which was directed towards the face and the root of the welded joint.

It is important to keep in mind that one main factor influencing the γ-FCC to ε-HCP martensitic transformation is the temperature reached by the material and its subsequent cooling rate, provided that the latter is directly dependent on the difference between peak temperature and the temperature at which formation occurs. Alongside with is, other factors, such as the accommodation of thermal stresses combined with the residual stresses left on the microstructure after cooling, are also important to consider since the indirectly supplied mechanical work lowers the driving force necessary for ε-HCP to form [29]. As such, the higher amount of ε-HCP on the HAZ is justified by different factors (i.e.,

Table 2
Phase fraction distribution along the weld microstructure, calculated using ImageJ on a representative location of each region.

Weld region		BM	HAZ	FZ
Phase fraction	γ-FCC	55.5%	42.5%	71.1%
	ε-HCP	44.5%	57.5%	28.9%

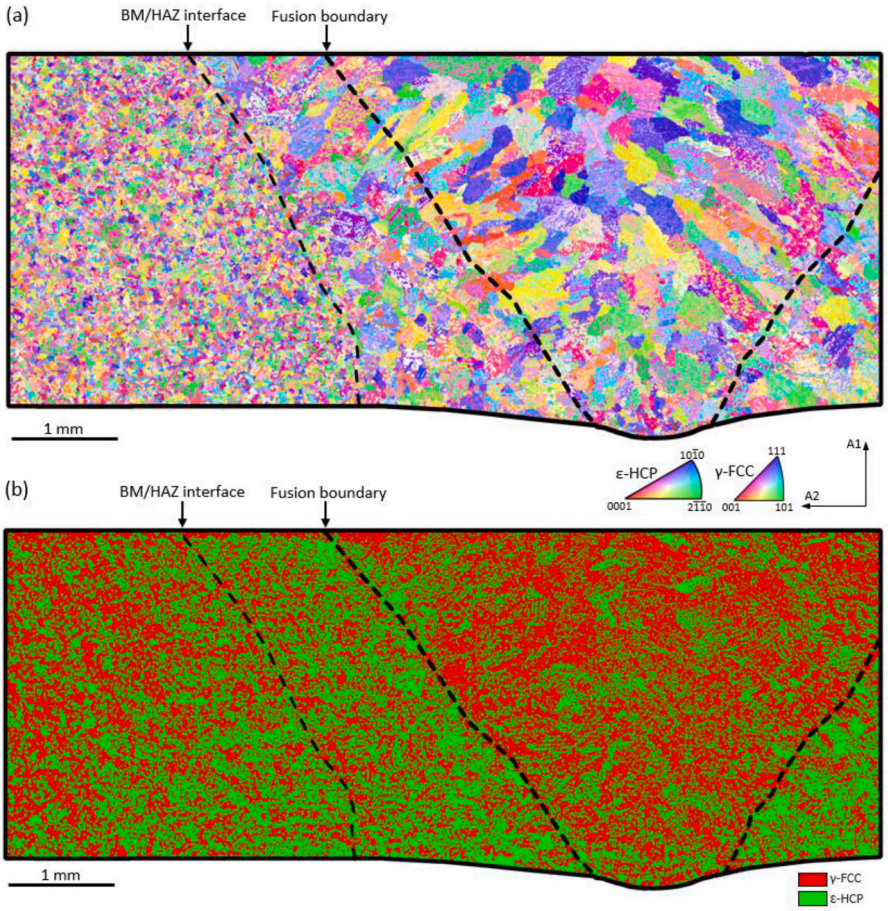

Fig. 3. Weld microstructure analysis: (a) IPF map and (b) Phase map.

peak temperature and stresses occurring on the HAZ) acting to produce an ε-HCP-richer region at this location of the joint.

The significantly lower phase fraction of ε-HCP in the FZ can be explained by the fact that in this region the material endured total remelting, allowing for new grains to form. The formation of ε-HCP is related to the lattice defects induced during solidification [30]. While transitioning to a solid phase and losing thermal energy, the atoms present in liquid arrange themselves into an ordered arrangement. However, in this process, defects can arise in the crystal lattice, due to a variety of factors, such as variations in cooling rates or impurities, disrupting the regular stacking sequence of atomic planes and leading to the formation of stacking faults. Eventually, these stacking faults coalesce resulting in the formation of thin plates of ε-HCP, by the gliding of Shockley partials of the 1/6 <112> Burgers vector. As such, the presence of this thermally induced ε-HCP is often commonly found in this HEA, and occurs as a means of relaxation of the thermally induced stresses generated during solidification. It is only with the application of an external stress that these structures will act as nuclei for the mechanically induced ε-HCP, via the TRIP effect [31–33].

Beyond this, one relevant factor that must be assessed is the influence of the parent γ-FCC grain size in the lower fraction of ε-HCP observed on the FZ. Liu et al. [34] related the γ-FCC grain size with the nucleation of ε-HCP, stating that the larger γ-FCC grain size, the easier it is for the martensitic phase to form, given that ε-HCP tends to nucleate around grain boundaries and grow towards the center of the γ-FCC grains. They also concluded that with grain refinement the formation of ε-HCP can be hindered, which translates into a decrease of grain boundaries, that have previously been assigned as primary nucleating sites for the ε-HCP phase. This fact, indeed, is in line with the larger amount of ε-HCP observed in the HAZ, where the grain size is larger. Nevertheless, the same conclusion cannot be reached in the FZ, where the γ-FCC grain size is at its higher values. As it is noticeable that the ε-HCP phase fraction variation is directly dependent on the ε-HCP grain size present within each region. That is, the higher phase fraction of ε-HCP also corresponds to larger thickness of the ε-HCP laths in the HAZ region (approximately 11.9 ± 1.7 μm), especially when compared to the FZ (5.8 ± 1.6 μm) and the BM (5.1 ± 2.5 μm).

For understanding the lower phase fraction of ε-HCP on the FZ, one must consider the dynamics associated with the solidification process and heat transfer that occurs during the solidification of the molten pool in non-equilibrium processes as in welding. As previously noted, the FZ is comprised of large dendritic grains with a high directionality towards the topmost center of the weld, which occurred due to competitive grain growth. Such process occurs from the HAZ/FZ interface, where the molten pool begins to solidifying and new grains start developing towards the center of the FZ, where the material experiences the higher temperatures and is still at the liquid state. At the same time, stacking faults may develop within the already solidified γ-FCC lattice. Nevertheless, the localized high temperatures surrounding the grains, aided by the liquid material present at that stage during solidification, can ease the movement of atoms allowing them to correct themselves within the lattice, achieving a lower energy phase condition. Such can hinder the progressive accumulation and thickening of stacking faults required for thermally induced ε-HCP to nucleate, as the γ-FCC grains progressively grow.

For further analysis, high-resolution EBDS maps, detailed in Fig. 4, were performed to further characterize the microstructure of the BM and FZ. The difference in shape of the grains in the two regions becomes clearer now, with the BM possessing angular-shaped grains while in the FZ they possess a more elongated morphology, with these differences arising from the different conditions of their formation. Martensitic laths observed on both the IPF (Fig. 4 (a) and (d)) and phase maps (Fig. 4 (b) and (e)), detail that their thickness is larger in the BM, as it would be expected from the previously explained ε-HCP formation on the FZ.

The KAM maps detailed in Fig. 4 (c) and (f), corresponding to the BM and FZ, respectively, can be used to obtain a qualitative evaluation on the existing residual strains before and after welding. During welding there is a non-uniform expansion and contraction along the welded joint which generates thermal strains within the different regions of the join. Eventual distortions within the crystal lattice can be relieved by the formation of dislocations at the grain interfaces, which results on a type of subgrain boundary being formed, often referred to as geometrically necessary dislocations (GND) [26]. Considering the relationship between the misorientation angle and the GND density, it is possible to interpret the KAM data in the context of the distribution of residual strains within welds.

In both cases, it is possible to perceive that higher KAM values, which are associated with a higher GND density, occur at the γ-FCC/ε-HCP phase boundaries, reflecting the increased local tendency for accumulation of microstrain [35,36]. However, comparing both regions it is possible to perceive that the BM has a more homogenous distribution of the misorientation angle, with a tendency for it to increase at the geometrically shaped grain boundaries. Nevertheless, given the dendritic nature of the FZ aided by the fast solidification rate of the molten

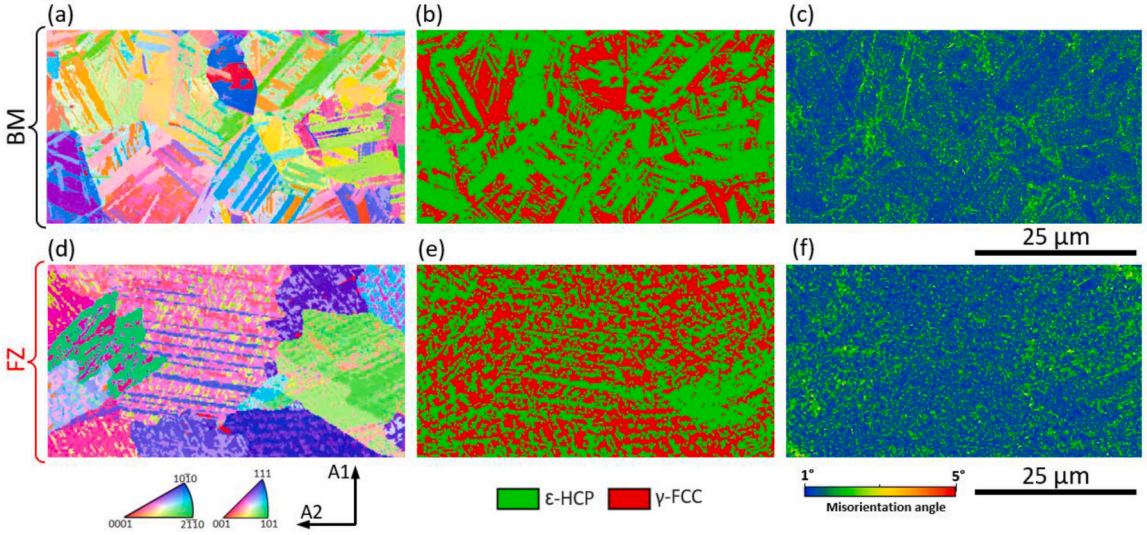

Fig. 4. High-resolution EBSD analysis of the BM and FZ. The IPF maps in (a) and (d), phase maps in (b) and (e), and KAM maps in (c) and (f) provide valuable insights into the crystallographic orientation, phase distribution, and deformation within the samples.

pool, a scattered misorientation level is present amongst the larger γ-FCC grains. This occurs especially given the smaller ε-HCP grain size and the consequent necessary accommodation of the different lattice structures, resulting on a higher accumulation of strain at the subgrain level. Such can contribute to a higher level of residual strain in the FZ.

3.2. Synchrotron X-ray diffraction

Fig. 5 displays representative synchrotron X-ray diffraction patterns taken from both the BM and FZ where the two principal phases, γ-FCC and the ε-HCP, are identified. The presence of Mn oxides in the microstructure can also be observed with a very low phase fraction, as it can be noted by the extremely low intensity of the associated diffraction peaks.

Although this representation of the existing phases in the BM and FZ can yield an insightful characterization of the sample, further analysis can be made by superimposing the diffraction patterns along the whole joint. Such can yield a good visualization of the differences that locally occur from one side of the BM to the other, due to the spatially varying weld thermal cycle. As such, synchrotron X-ray diffraction measurements were performed along the full extension of the welded joint. Fig. 6 (a) details a colormap of the full azimuthal integrated Debye-Scherrer rings, which takes into consideration all the data captured by the 2D detector from the analyzed spot. Here, is possible to obtain a qualitative observation on the variation of both peak intensity and width, where changes in the HAZ and FZ, compared to the original BM, can be related to thermal cycle conditions due to the intense heat generated by the electric arc during welding. Furthermore, the intensity and width variations are especially noted for the ε-HCP peaks (refer to Fig. 6 (b)).

Equivalent to this, a 3D depiction of the γ-FCC (311) and ε-HCP (10–13) diffraction peaks can be observed in Fig. 6 (b), allowing to obtain a better perspective on the peak shape evolution along the analyzed regions. The reason for the selection of these diffraction reflections is related to their insensitivity to intergranular strains [37]. To further understand the obtained synchrotron X-ray diffraction data, fitting of the γ-FCC (311) of and the ε-HCP (10–13) diffraction was performed to retrieve relevant peak parameters, namely the peak intensity and full width at half maximum (FWHM).

Starting with the peak intensity, this parameter can be related to the phase fraction of each phase, while also being strongly related to texture effects of the analyzed spots [38]. These results are presented in Fig. 7 (a) and are discussed next.

However, it is important to note that these values correspond to the normalized intensity (I/I_0, where I_0 is the peak intensity of the corresponding peak in the BM), thus a quantitative analysis of phase fraction cannot be inferred from this graph. Nevertheless, as the matrix phase in this HEA, the peak intensity variation of the γ-FCC shows a steady variation, while only a slight decrease is visible when reaching its minimum at the weld centerline. However, for the ε-HCP phase, the three weld regions are clear. Here an increase in intensity of about 1.8 times that of the BM can be observed in the HAZ, while an even higher increase is visible in the FZ, reaching about 5 times the intensity of the BM at its maximum, which highlights the variation in phase fraction and grain morphology (texture) along the welded joint. Although this variation in peak intensity cannot directly translate the phase fraction of ε-HCP, the reason for this increase in intensity in the HAZ, in comparison to the BM, can be indeed due to the thickness increase of the already present ε-HCP laths. This affects the texture of the HAZ due to the larger ε-HCP grain size, which results in a lesser number of grains diffracting the X-ray beam, although the present of larger grain size means that the diffracted intensity coming from a single grain will be significantly higher. Such factors influence the statistics of the representative ε-HCP phase diffraction peaks and consequently their intensity, resulting, in the present case, in an increase in peak intensity. However, the massive increase of intensity in the FZ cannot be explained by only that, since the amount of ε-HCP is lower in this region, as observed by electron microscopy. Thus, to understand this feature one must consider the local material texture that arises from the highly directional temperature flow during welding. Nevertheless, as this analysis only encompasses the full azimuthal integration of the Debye-Scherrer rings, another way to infer on this phenomenon is to evaluate the peak intensity vs FWHM plot (see Fig. 7), where in the FZ is possible to observe that the ε-HCP diffraction peaks are sharper (higher intensity) with less width (lower FWHM). Such can be translated into the fact that, although the newly formed ε-HCP grains have a lower grain size, these grains are highly oriented resulting in higher peak intensities in this region.

On a different note, the FWHM evolution translates the combined influence of microstrain, coming from structural defects, with the size of the smaller domains within a grain (crystallites) that can coherently diffract the incoming X-rays [38]. Such results are displayed in Fig. 7 (b).

Concerning the γ-FCC phase, different trends can be observed throughout the welded joint, allowing to easily separate the three

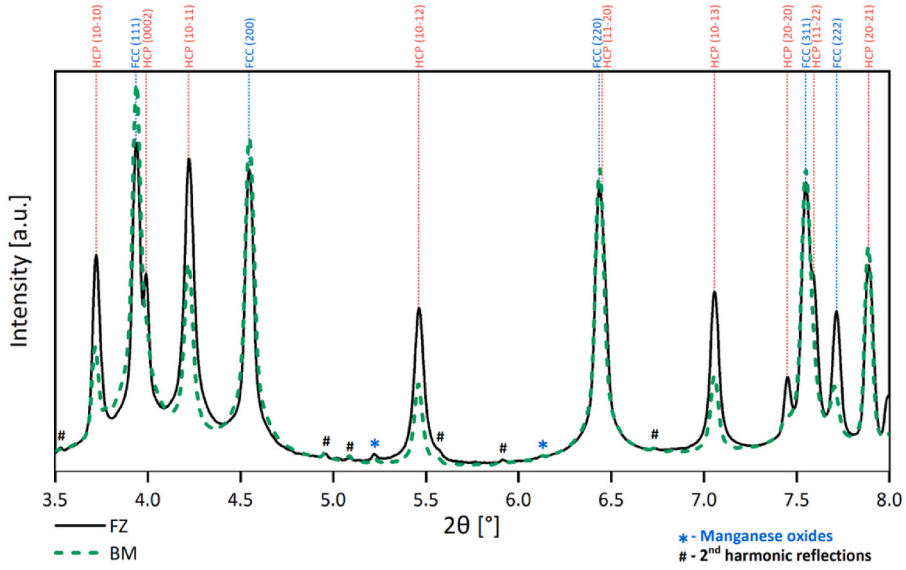

Fig. 5. Representative synchrotron X-ray diffraction patterns from the BM and FZ. The diffraction peaks corresponding to the γ-FCC and the ε-HCP phases are identified on the top. Lower intensity reflections corresponding to manganese oxides (*) and 2nd harmonic reflections (#), the latter resulting from the beamline setup, are also identified.

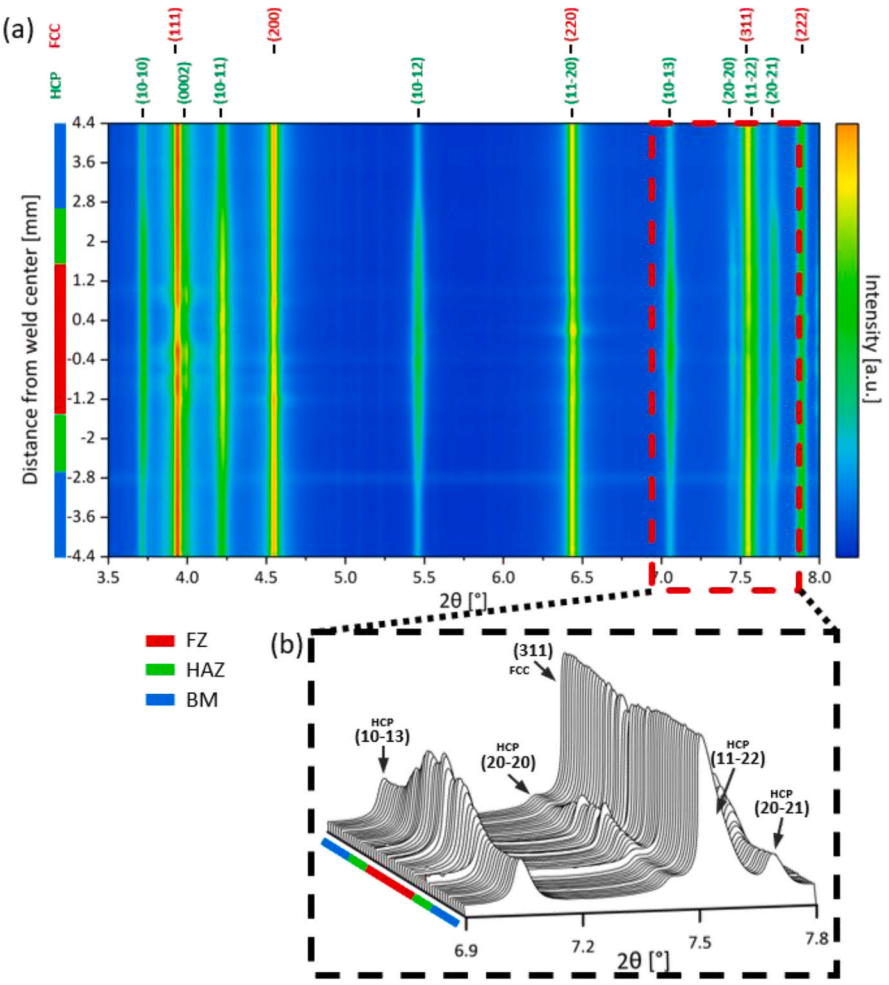

Fig. 6. – Synchrotron x-ray diffraction mapping: (a) colormap exhibiting the variation of the diffraction peaks after full azimuthal integration; (b) 3D depiction highlighting the diffraction peaks within the 6.9–7.8 2θ range.

typical regions of a fusion weld (BM, HAZ and FZ). Going from the approximately constant behavior in the BM, the FWHM exhibits a slight increase followed by a sudden decrease marking the position of the HAZ. This decrease is then followed by an accentuated increase, where the FZ can be identified. A mirrored behavior can be observed detailing a symmetry axis along the weld centerline, as expected since autogenous welding was performed in this work. On the other hand, the ε-HCP phase exhibits a different trend. In this case, beyond the nearly constant FWHM on the BM and decrease when reaching the HAZ, the FZ exhibits a fluctuation at the lower level of values. With complementary knowledge coming from the previous optical and electron microscopy microstructural analysis, it is possible to correlate grain features with the synchrotron data, especially concerning the HAZ. As mentioned, this region experienced the effect of recrystallization and grain growth phenomena which is clear on the FWHM evolution throughout the weld. That is, as it is possible to observe via optical microscopy (refer to Fig. 2) the extension of the HAZ is roughly 1 mm. However, in the case of the FWHM the extension of the HAZ reaches approximately, 1.5 mm in each side of the FZ, highlighting the recrystallization phenomena that occurred during the welding process, beyond the visible effect of the grain growth on the microstructure.

Setting the BM as the standard for comparison, where a steady behavior can be observed for both phases, the decrease in FWHM occurring in both phases can come from the residual stress relaxation conditions arising from the high temperatures experienced during welding associated to the relatively low cooling in the HAZ. Here, the higher amount of the martensitic phase ε-HCP, which can be a direct result of the cooling rate, can result on a region with a lesser amount of structural defects by allowing the atoms to readjust on the lattice. Additionally, recovery mechanisms may also take place during the permanence time a high temperature, in which case relieving of the microstrain developed upon welding is attained. These factors result in a region where the FWHM decreases on both phases.

On the FZ, the fraction of γ-FCC and its grain size is visibly higher when compared to the BM (refer to Fig. 4). While the probability for more structural defects to occur in the γ-FCC phase is increased in the FZ, due to the massive development of large dendritic grains in a short time period, the effect of grain size in the FWHM is also worthy of discussion. As such, the dynamic thermal gradient (G) that takes place in welding is relatable to the growth rate (R) in terms of the microstructure that develops upon solidification of the molten pool. The combined action of both G and R, under the previously discussed GTAW welding conditions, results on a microstructure comprising grains that tend to develop rapidly during solidification. Therefore, small differences between the atomic arrangements of the atoms are to be expected amongst the dendrites and the solidifying interdendritic space. Such can result on small crystallographic deviations between grains of the same crystal structure, which in turn may result in minor differences on the diffracted peak positions. These small-scaled differences, when added together by the coherent diffraction volume of the incoming X-ray beam, can influence the peak shape in a manner that the smaller they are, the larger the value of the FWHM associated to a certain peak. As such the impact of (smaller) sub-grain structure size translates into the higher FWHM of the γ-FCC phase in the FZ, as the refined grains (as part of the

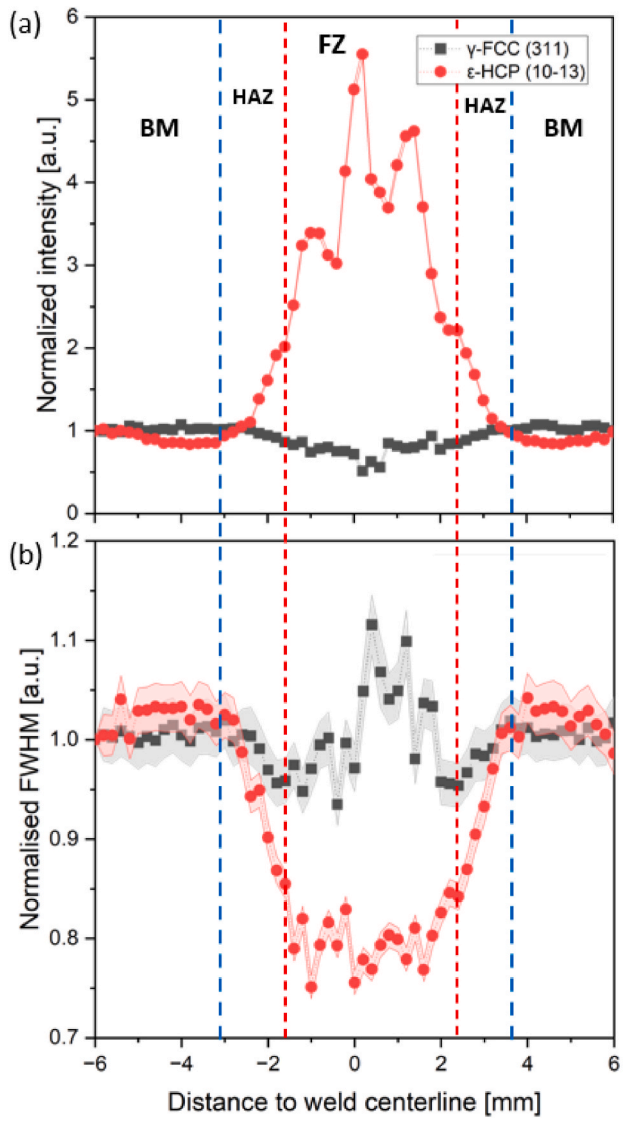

Fig. 7. Evolution of (a) peak intensity and (b) full width at half maximum along the welded joint.

solidification substructure) that develop within the γ-FCC grains during the fast cooling of the weld are different, in size, from the grains that develop during the slower cooling of the BM upon casting. Likewise, the same does not occur for the ε-HCP phase, which exhibits only a decrease on it FWHM with a large fluctuation of values in the FZ. In summary, the different FWHM values exhibited throughout the weld regions depend simultaneously on competition between microstrain and grain size developed, with for the latter the sub-grain structure size being of primary importance.

Furthermore, beyond the different grain sizes visible throughout the microstructure in Fig. 2, it is possible to quantify the microstrain within the microstructure, via the Williamson-Hall method. This method allows to separate the influence of the microstrain and the size of the sub-grain structures on the FWHM. Therefore, after removing the instrumental apparatus influence on the FWHM, it is possible to separate the contribution of both factors on this parameter and finally provide a quantification of the microstrain distribution on the sample. The procedure for this calculation is detailed in Ref. [39] and the results are exhibited in Fig. 8.

As an averaged contribution of the peaks on the diffraction patterns, it is again possible to observe the distribution of microstrain along the full extension of the weld. In both cases the BM exhibits the steadiest behavior, while the remaining regions of the weld showcasing a more scattered distribution of values. Considering the γ-FCC phase, the microstrain exhibited by the BM is characterized by a value of 2457 ± 577 με, reducing in value in the HAZ and reaching its minimum in the FZ, corresponding to 949 ± 741 με. In the ε-HCP phase, however, the BM exhibits a microstrain of 1341 ± 457 με, which also reduces when reaching the HAZ. The microstrain distribution in the FZ behaves differently from the γ-FCC, reaching a maximum of 1872 ± 1966 με and a minimum of 118 ± 841 με. Such distribution is with good agreement previous EBSD microstructural analysis.

However, full azimuthal integration of the Debbye-Scherrer rings is not sufficient to fully evaluate the microstructure evolution of the different regions of a welded joint, as the orientation-dependent microstructure changes are averaged [7]. To overcome this, partial integration of the Debbye-Scherrer rings enables the identification of such orientation-dependent changes. Fig. 9 details the evolution of the diffraction patterns on the 6.9 to 7.8 ° 2θ range, after using a 1-degree integration step along the azimuthal angle. The analyzed 2θ range is the same as that shown in Fig. 9 (b), allowing to observe the evolution of both the γ-FCC (311) and the ε-HCP (10–13) diffraction peaks in the BM, HAZ and FZ. Furthermore, quantification of the peak center with respect to the azimuthal angle of the (311) and (10–13) planes is also presented to showcase the different microstructural features occurring in the γ-FCC and the ε-HCP grains, respectively.

In these azimuthal angle vs diffraction angle plots is possible to see how the peak position changes along the azimuthal angle. In a non-textured and stress-free condition, the peak position would be kept constant all along the azimuthal angle (as it occurs with LaB_6 calibration powder, for example). However, this does not occur in any of the regions of the joint (BM, HAZ and FZ), being an indication of the existence of both texture and stresses across the material. From a texture perspective, it can be observed an overall trend in all cases for the peaks to deviate to lower 2θ values from the averaged value when near the azimuthal angles of 90 and 270°, which is the direction perpendicular to the fusion boundary, where preferential growth occurs during solidification of the molten pool. The opposite behavior, i.e., a shift of the peak position to higher 2θ values, corresponding to a decrease in the interplanar spacing, occurs for the 0 and 180° angles. It should be mentioned that a positive shift in 2θ, corresponds to a decrease in the interplanar spacing and suggests the development of a negative microstrain for the 0 and 180° azimuthal angles. The opposite occurs for the 90 and 270° azimuthal angles. Although, qualitatively, the FZ presents the same behavior as that of the BM and HAZ (refer to Fig. 9), the colormap pattern corresponding to this region (refer to Fig. 9 c)) evidences a high variation on the diffraction peaks, resulting in areas on the Debbye-Scherrer rings where no peaks are observable. This evidence the effect of large grain size combined with the preferential texture developed on the microstructure upon solidification of the molten pool. Alongside with this, the peak center distribution in Fig. 9 (f) and (i) do not follow a steady alignment as in the BM or the HAZ, as expected from the microstructure of the FZ, which can be an indication of non-uniform strain distributions, owing to the non-equilibrium cooling conditions experienced by this region of the joint. However, the peak center variation still showcases the same positive and negative variations in 2θ along the azimuthal angle, translating in microstrain differences, which are azimuthal-dependent.

For reference, here the microstrain, ε, which is calculated from a representative peak of each phase, is defined by Equation (1):

$$\varepsilon = \frac{d - d_0}{d_0} \quad (1)$$

where d is the interplanar space of the analyzed diffraction plant and d_0, corresponds to the interplanar space in a stress-free condition. Although d_0 is not defined in this case, as its determination is difficult [40] and outside the scope of this work, it is reasonable to assume that d_0 takes

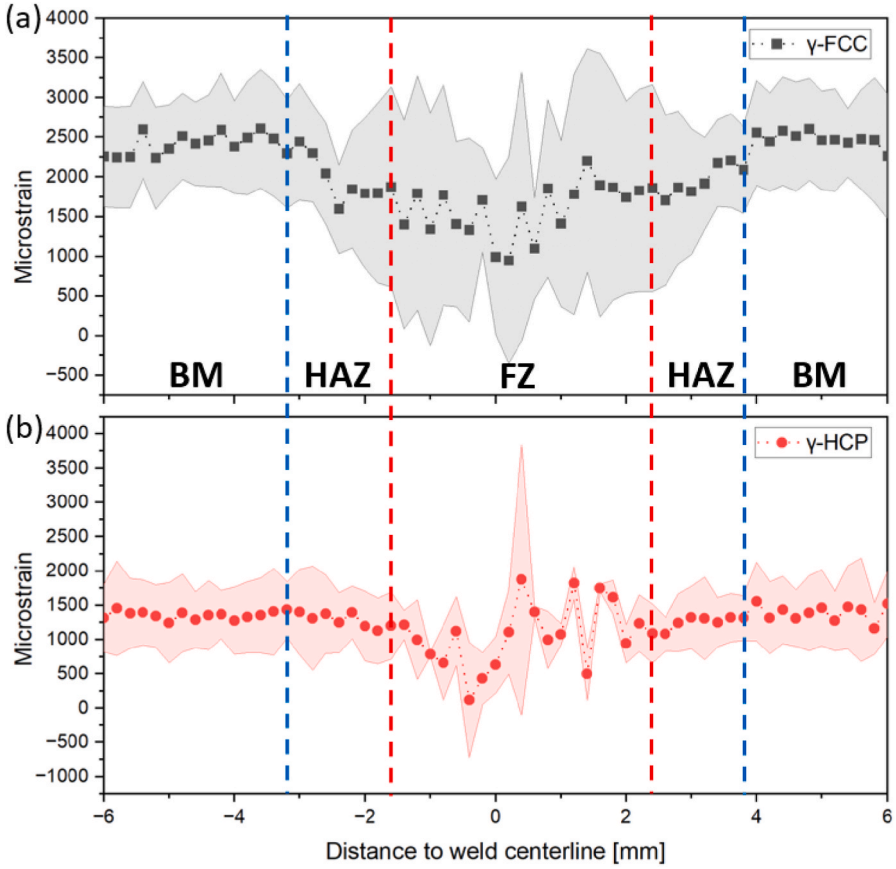

Fig. 8. Distribution of microstrain on the (a) γ-FCC and the (b) ε-HCP phases along the full extension of the weld.

the average value in between the minimum and maximum shift for each peak. For the (311) γ-FCC phase, the higher variation on 2θ was obtained in the FZ, with a variation of 0.092° (corresponding to a microstrain of ≈6400 με), while the lower variation was exhibited by the HAZ with 0.081° (microstrain of ≈5500 με). For the ε-HCP (1013) peak, a similar behavior can be observed where the FZ (with a variation of 0.096° and microstrain of ≈6800 με) attains the higher difference and the HAZ has the lower amount, with a variation of 0.083° (microstrain of ≈6100 με). Such values allow to conclude that concerning the 2θ variation (and consequently the microstrain), the HAZ has the most stable behavior when compared to the other regions of the weld. Such can be related to the higher amount of ε-HCP phase in this region, whose formation contributes to the reduction of internal strains developed by cooling and concurrent solidification of the adjacent molten pool. Such agrees with the data obtained with the KAM maps.

3.3. Thermodynamic simulations

Beyond the performed microstructure analysis, understanding the solidification path occurring in terms of the decreasing temperature on the FZ can provide significant knowledge within a simulation/predictive basis. Such can be obtained through CalPhaD (Calculation of Phase Diagrams) calculations that can offer a consistent description of the microstructure to be expected when the liquid material finally reaches the solid state under non-equilibrium conditions. As such, to predict such solidification path, one can use the Scheil-Gulliver methodology [41,42] instead of standard equilibrium phase diagrams. This method can be used for predicting the solidification behavior in non-equilibrium conditions by distinguishing the composition of the newly formed dendrites from that of the interdendritic fluid that surrounds them.

Fig. 10 details the solidification path using the Scheil-Gulliver calculations following the CALPHAD-based methodology. Contrary to what would have been expected from the joint microstructure, the results indicate that only the disordered γ-FCC and σ phases are expected to be formed during solidification. Nevertheless, three stages are visible on the solidification path. Upon descending from the liquidus temperature, the first stage comprises a liquid to σ phase transformation. When reaching ≈1353 °C, γ-FCC starts to form characterizing the beginning of the second stage of the solidification path, where the solidification curve starts to deviate from that associated with the equilibrium curve (dashed line in Fig. 10). The third stage, however, occurs at ≈1257 °C, where σ phase is no longer thermodynamically stable, finally resulting on a microstructure composed only by γ-FCC. The formation of σ however, is debatable since the development of this phase in the microstructure usually occurs after long time exposure at high temperatures [43]. Moreover, no evidence of such phase was observed in the high energy synchrotron data of the present work, which may suggest that the undercooling experienced by the melt pool does not enable the formation of σ phase but rather of a metastable γ-FCC as the primary solidification phase.

Contrary with what would be expected considering the Scheil-Gulliver calculations, the presence of ε-HCP in the weld joint requires that this thermodynamical analysis must account for other conditions, such as chemical and non-chemical factors that can alter the Gibbs free energy of formation of ε-HCP, rendering it more thermodynamical stable than the γ-FCC.

Considering chemical factors, the previously detailed EDS analysis (refer to Fig. 2) showed that solute redistribution among the dendrites and the interdendritic fluid in the FZ occurred in a somewhat uniform way. However, the HAZ which did not endure any chemical changes capable of altering its microstructure, as demonstrated in the phase map displayed in Fig. 3 (b), exhibiting a higher amount of ε-HCP, and the same can be said concerning the BM. Therefore, to understand the solidification and possible solute segregation from the newly formed

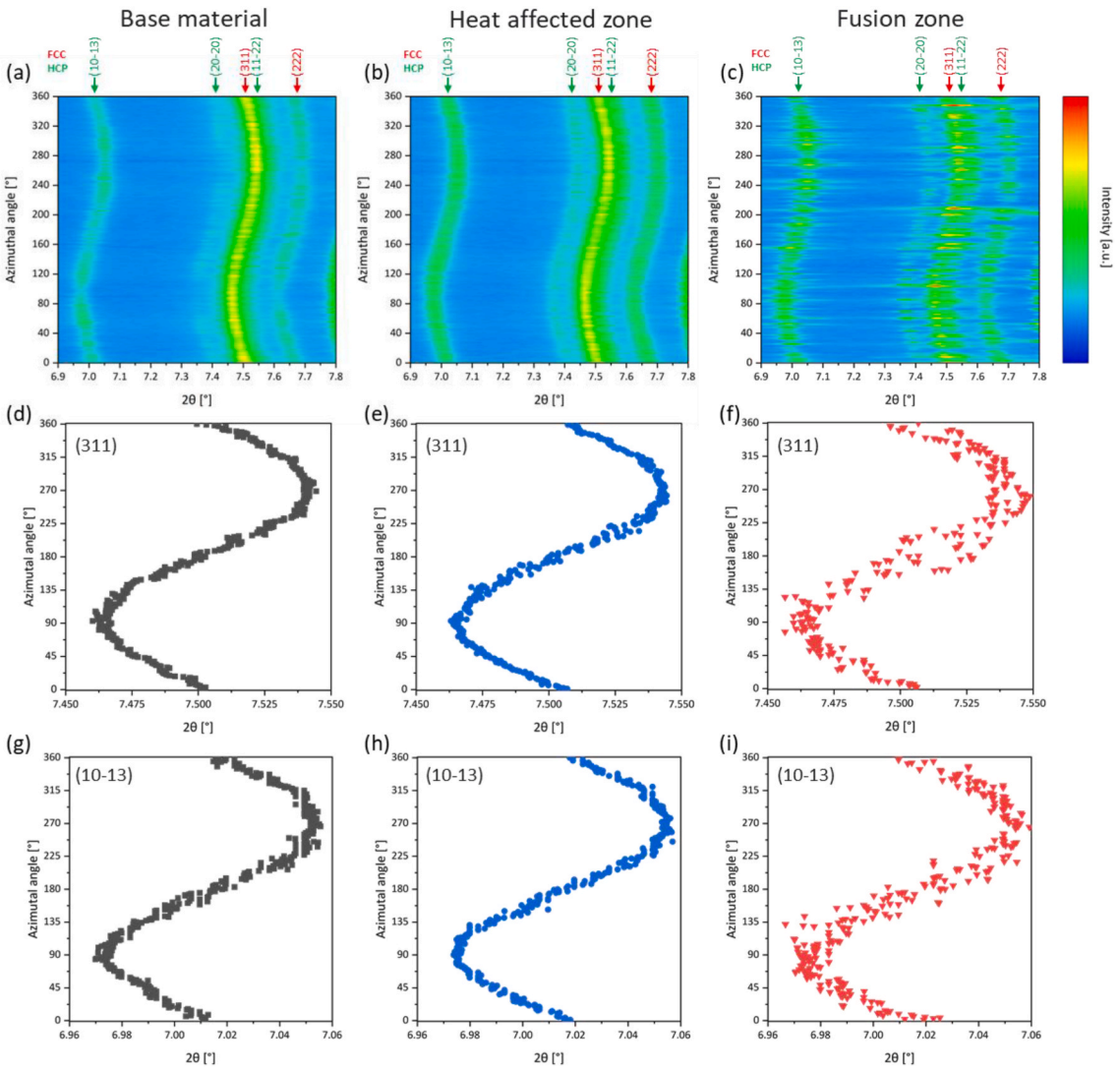

Fig. 9. Evolution of 2θ angle obtained by integrating in 1-degree segments along the azimuthal angle on representative zones of the: (a) BM, (b) HAZ and (c) FZ. On each region, peak fitting was performed on: the (311) peak of the γ-FCC (d), e) and f)) and on the (10–13) peak of the ε-HCP phase (g), h) and i)).

dendrites to the interdendritic fluid, the partition coefficients of the γ-FCC phase regarding the composition of the liquid, are displayed in Fig. 11. The partition coefficient, k, allows to infer on the variation in composition of the liquid throughout the solidification enabling to understand which elements tend to segregate to the interdendritic fluid and which remain stable within the dendrites. Here it is possible to understand that when solidification starts Mn, Co and Cr elements all have a $k < 1$, meaning that these elements are prone to be stable in the dendritic core. The same, however, does not occur for Fe, which remains well above 1 during solidification. Such indicates that Fe is being segregated into the interdendritic fluid, not contributing as much as the other elements for dendritic formation. At the last stages of solidification, it is also noticeable that for Cr k rises above 1, being segregated alongside with Fe. Overall, an increasing trend can be observed in all elements, except for the Co curve, which indicates that the amount this element is less available for the further formation of the γ-FCC matrix phase.

Nevertheless, non-chemical factors also play a key role in the formation of ε-HCP. Beyond the mechanism of formation thermally induced ε-HCP through stacking faults, where phase transformation can occur to relax stresses induced by thermal strains. Such internal strains are associated to the thermal cycle characteristic of fusion welding that can be left in the weld by the conjoined influence of the peak temperature experienced in the HAZ, combined with the cooling rate, which tends to be high in arc-based welding. Furthermore, another topic that should be assessed it the variation in Gibbs free energy between the ε-HCP and the γ-FCC phases. For this analysis Fig. 12 displays the Gibbs free energy (G) curves of the γ-FCC and ε-HCP phases, on the 300 °C–1100 °C temperature range. Here, the G(ε-HCP) curve corresponding to the metastable phase is higher than the G(γ-FCC) one which corresponds to the matrix stable phase exhibited by the DP-HEA, such being compliant with the results exhibited in Fig. 10. Nevertheless, the probability for the stabilization of the ε-HCP phase in the microstructure can be qualitatively assessed by subtracting the G(γ-FCC) to the G (ε-HCP) curves. The result is displayed in Fig. 12 (b). As it is possible to observe the difference between G(ε-HCP) and G(γ-FCC) decreases as the temperature drops, making it easier for ε-HCP to form in the weld microstructure. That is, although the γ-FCC is more prone to occur, comparing the order of magnitude of the G(γ-FCC) curve with the descendent tendency that the G(ε-HCP) - G(γ-FCC) curves show, it is possible to infer that the probability for ε-HCP to form amidst the γ-FCC matrix is relatively high. Nevertheless, it is important to keep in mind that the martensitic transformation, having a thermal or mechanical nature, still requires an additional driving force to overcome the energy barrier that tends to decrease with decreasing temperature for the ε-HCP to develop within the weld microstructure.

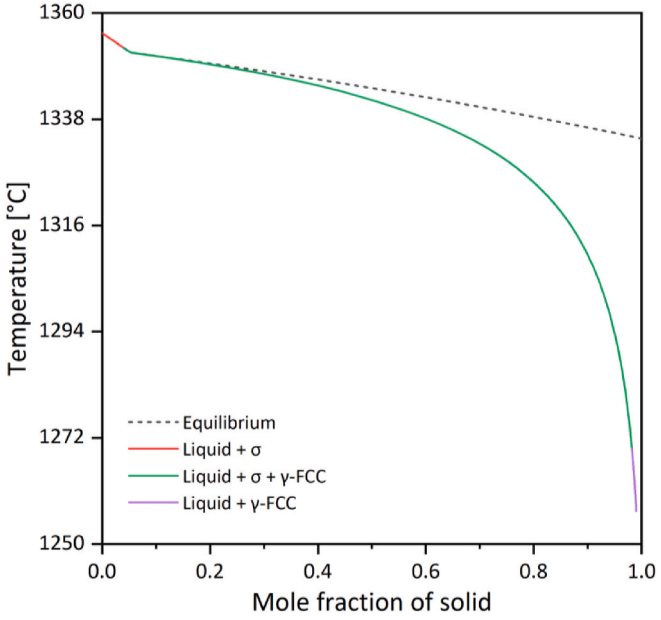

Fig. 10. Scheil calculations performed considering the nominal composition of the HEA base material.

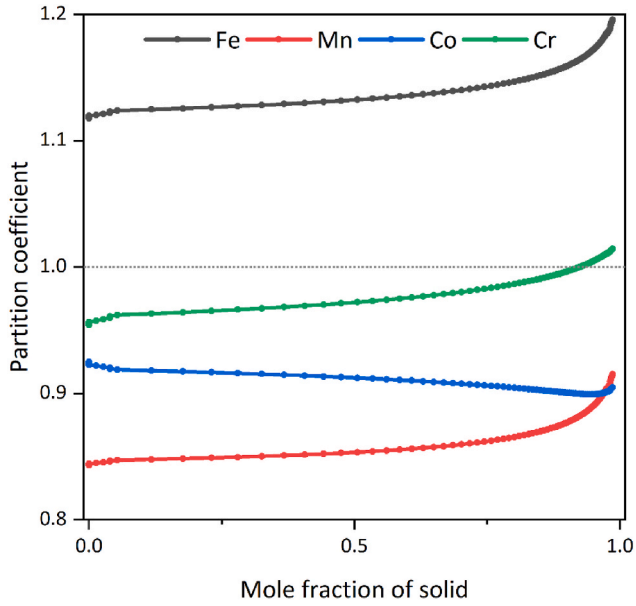

Fig. 11. Partition coefficients of the matrix γ-FCC phase during solidification, calculated from the data obtained from the calculations obtained with the Scheil-Gulliver method.

3.4. Mechanical performance of the welded joints

From an application standpoint, analyzing the joint's mechanical behavior is of importance since it can provide a reliable way to evaluate the suitability of the material as a structural component.

Fig. 13 (a) details the microhardness mapping performed on the welded joint comprising all regions of the weld. Here, it is possible to observe that the BM exhibited the lowest values of microhardness, around 174 $HV_{0.5}$, while a constant increase culminating in the middle region (FZ) of the analyzed cross section, with approximately 239 $HV_{0.5}$, can be observed. As such, other than what should have been expected from the larger grains of the softer γ-FCC phase, the higher hardness values were obtained in this region, which contradicts what should have been expected according to the phases that comprise this DP-HEA. One factor that can be accounted for such to occur is the subsequent martensitic transformation that occurs upon plastic deformation (imposed by the indenter during hardness measurement), given the TRIP effect characteristic of this HEA, which may render some inaccuracy on this type of measurements.

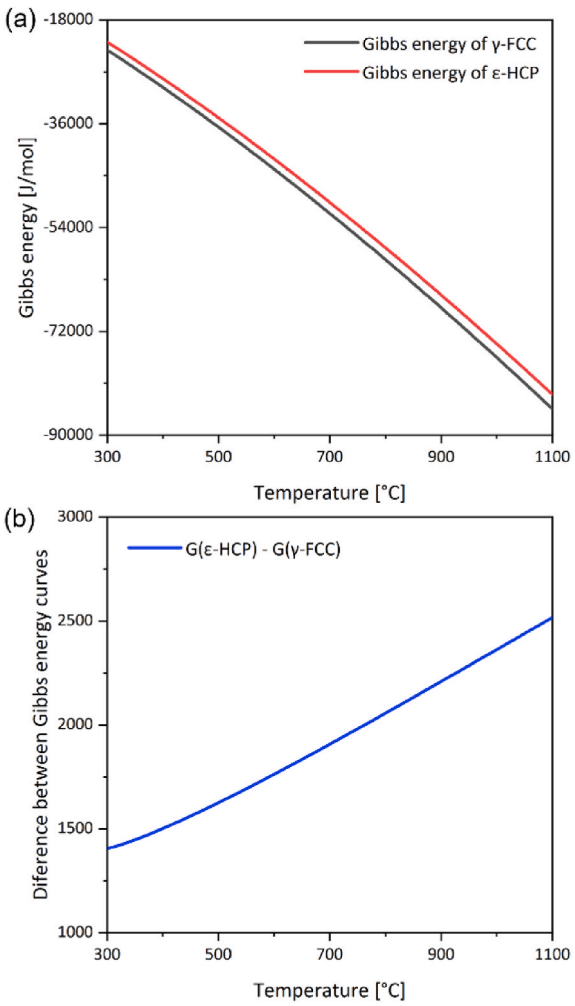

Fig. 12. Analysis of (a) Gibbs energy of the γ-FCC, ε-HCP and Liquid phases and (b) difference between the Gibbs energy curves of the ε-HCP and Liquid phases and the matrix γ-FCC phase.

Nonetheless, provided that the composition remains approximately constant throughout the weld, this variation on the microhardness can also be explained in terms of grain size, as well as existing phases and their volumetric fractions. Additionally, as both phases are widely present in all regions of the weld, one possible reason for the results displayed in the microhardness map is especially dependent on the grain morphology of the harder ε-HCP phase and its conjugation with the softer γ-FCC phase. However, the BM possesses the lower values of hardness across the joint, although this region of the material has a smaller γ-FCC grain size. Here, several factors, such as grain morphology and phase fraction, may yield different effects on the mechanical behavior of the material. According to the Hall-Petch equation, smaller grain size translates into increased strength. Nevertheless, as the grain increases in both the HAZ and FZ, and the hardness of these locations is higher than in the BM, one possibility is that the volume phase fraction of ε-HCP compared to γ-FCC plays a significant role on the hardness measurements. Such implies that the increased volume fraction of ε-HCP phase contributes in a more substantial way to increase the hardness at both the HAZ and FZ. Conversely, opposite results are observed in the

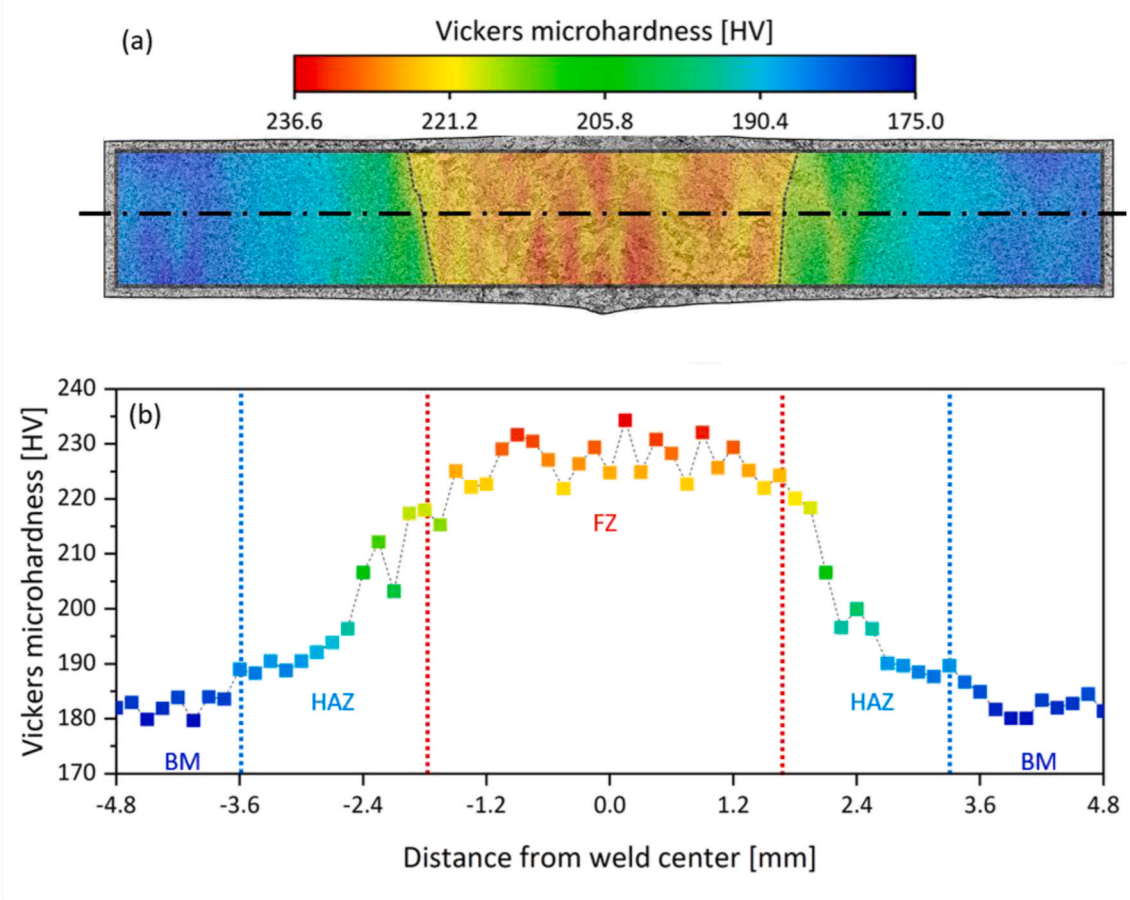

Fig. 13. Microhardness evaluation of the welded joint: a) mapping of the variation of hardness along the full extension of the weld superimposed with optical microscopical results and b) representative hardness evolution taken from the middle line of the map.

FZ, where the phase fraction of the ε-HCP is lower and so is it size. Here, the strengthening effect induced by the reduced grain size of the ε-HCP phase is significantly higher than that of the γ-FCC, thus although there is a decrease in the volume fraction of the ε-HCP phase, its lower grain size significantly aids in increasing the material hardness at the FZ.

Consequently, as readily observable in Fig. 13 (b), which correspond to the measurements taken at half the thickness of the joint, the microhardness in the BM is stable starting to increase when entering the HAZ, which has a slightly larger ε-HCP phase fraction in its microstructure. In addition, the larger hardness values appear in the FZ where the ε-HCP exhibits its smaller grain size.

Fig. 14 displays representative tensile data of the welded, benchmarking against the BM. Overall, the welds fractured at a final strain of 17.6 ± 1.7%, achieving a maximum tensile stress of 717 ± 36 MPa. In comparison, the BM had a tensile strength of 749 ± 32 MPa and fracture strain of 30.5 ± 7.7%, all engineering values. Therefore, the welded samples reached 96% of BM strength, while preserving nearly 58% of its ductility. The reduced ductility of the welded joints can be ascribed to the microstructural variations present in the weld. As previously discussed, the microstructure (spatially varying grain size and volume fraction variations), as well as the residual stress conditions of the weld have a major influence on the individual behavior of each analyzed region resulting, in total, on different mechanical response between the weld and the BM.

To extrapolate how different is the tensile behavior of each region of the weld during macroscopic tensile solicitation, DIC was performed, and these results are displayed in Fig. 15. As can be observed, the BM and the FZ exhibited the lowest elongation of 16.4% and 14.4%, respectively, before fracture occurring in the HAZ. The maximum

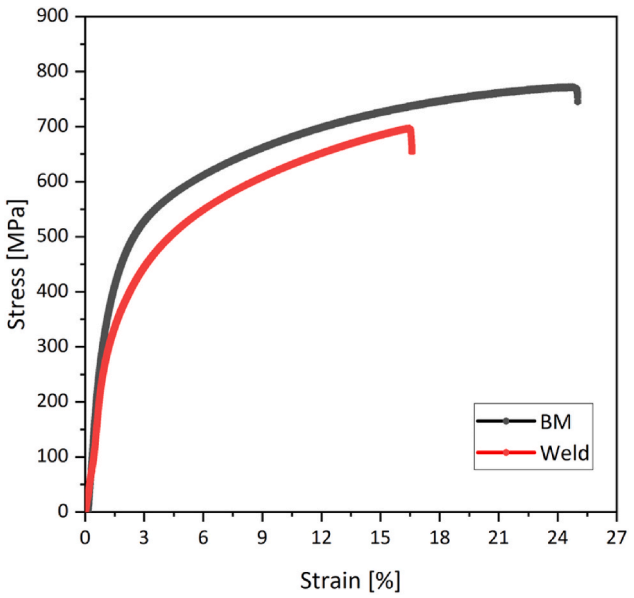

Fig. 14. Tensile test behavior comparison between the BM and the welded joints.

elongation, however, was observed in the HAZ, reaching 29.0%.

The reason for this behavior can be expected by the combined effect of microstructural differences and the microhardness variation exhibited throughout the weld. While the FZ is the region with the largest grain

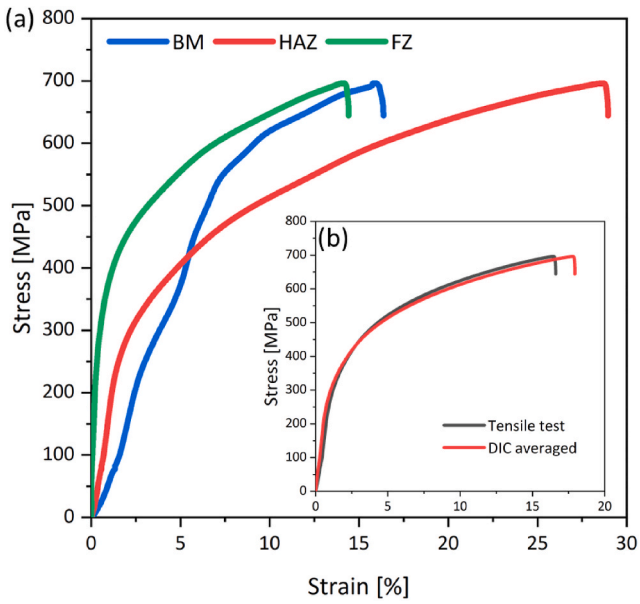

Fig. 15. Stress-strain behavior of: (a) representative points located in the BM, HAZ and FZ obtained with DIC during tensile testing of the welded joints and (b) welded joint and the DIC average response.

size, it is also the region that exhibits a higher hardness. Such can be related to the higher amount of γ-FCC, which transforms into ε-HCP via the TRIP with plastic deformation, alongside the ε-HCP smaller grain size, granting it a stiffer behavior than the other regions. On the other hand, the BM exhibits a similar behavior to the FZ, although with showcasing a higher ductility, which was expected from the microhardness measurements combined with the effect granted by the small and equiaxial grain size with multiple ε-HCP nuclei within, ready to develop into larger ε-HCP lathes. Furthermore, the behavior exhibited by the HAZ can be due to the combined effect of larger grain size that this region exhibits when compared to the BM, and the relatively lower hardness when compared to the FZ, although exhibiting a higher fraction of the martensitic ε-HCP phase. Furthermore, we would like to point out that the γ-FCC to ε-HCP transformation rate in each region, should be a topic of interest to discuss for further analysis in subsequent works.

Analysis of the joint's fracture surface in detailed Fig. 16, where evidence of a ductile-like fracture can be observed, as validated by the large and homogeneously distributed dimples. The presence of small particles can also be observed in the close-up view of Fig. 16 (b). These particles were previously reported by Hossain et al. [44] on the fracture surface of tensile samples as containing high content of Mn. These correspond to the Mn-rich particles scattered within the microstructure pointed out in Fig. 2 (e) and identified via synchrotron X-ray diffraction in the present study. Other features, such as the cleavage markings, highlighted in yellow, can also be observed as they are characteristic of localized brittle fracture caused by the presence of the ε-HCP phase in the microstructure, alongside with the larger dimples resulting from the more ductile γ-FCC phase.

It is, nonetheless, proved that processing this DP-HEA through welding leads to a material with intense microstructural variation throughout the regions that comprise the joint, although macroscopically it was possible to achieve a mechanical performance similar to that of the base material. Future work will assess the role of heat treatments on these welded joints targeting an improvement on their mechanical behavior.

4. Conclusions

The present study delves into the investigation of the weldability of an as-cast $Fe_{50}Mn_{30}Co_{10}Cr_{10}$ DP-HEA. This HEA's main characteristic is the TRIP effect, in which the matrix γ-FCC phase transforms into the martensitic ε-HCP upon the application of an external stress. Nevertheless, the presence of ε-HCP on the microstructure can also be of a thermal nature, being formed because of stacking faults coalescence.

Having observed the excellent weldability via GTAW on the present DP-HEA, where defect-free welds were obtained, the current work explored the correlation between microstructure and mechanical behavior of GTAW welded joints. As such, it was possible to derive the following major conclusions.

(1) Microstructurally, quantification of grain size and phase fraction fluctuations of the γ-FCC and ε-HCP phases, using multiple characterization methods, allowed to observe the differences between the weld regions which is attributed to the spatially varying thermal cycle. No evident chemical differences were found within the weld, beyond the presence of Mn-oxides at a lower fraction.
(2) Beyond grain size variations, EBSD data revealed distinct phase distribution along the joints between the two major phases that compose this alloy. While the BM exhibited the higher amount ε-HCP, the FZ proved to be richer in the γ-FCC phase.
(3) Synchrotron X-ray diffraction allowed to identify the γ-FCC and the ε-HCP phases, permitting also to confirm the presence of Mn-oxides. Further analysis was performed to investigate the stress

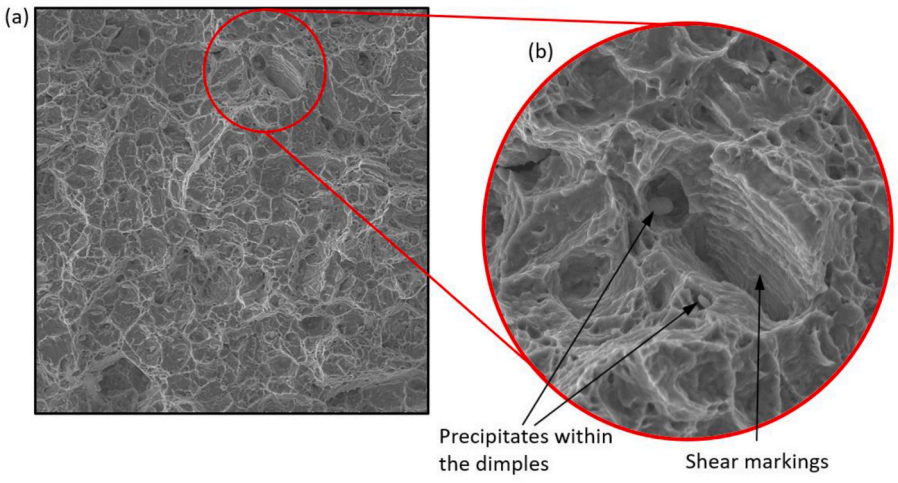

Fig. 16. Fracture surface after tensile testing inspected by SEM: a) Overall Overview and b) detailed view of the fracture surface.

conditions of the regions that comprise the weld by means of peak analysis of the synchrotron data. Lower values for microstrain were observed on the FZ, while the HAZ showcased a more uniform strain distribution.

(4) Thermodynamic calculations, using the Scheil-Gulliver model, evidenced the formation of γ-FCC from the Liquid. The formation of σ was also predicted, although no trace of it was found in the welded joints, likely due to the undercooling that occurs within the FZ. No indication of σ phase was found in the synchrotron x-ray diffraction patterns.

(5) No evidence of the TRIP effect was observed, being the ε-HCP present in the welded joint a result of the thermal cycles induced by the GTAW process.

(6) Considering the mechanical behavior, the FZ exhibited higher hardness values while the BM exhibited the lowest. Overall, the tensile tests indicated that the welds could endure stresses up to 717 ± 35.7 MPa at a 17.6 ± 1.65% strain, which corresponds to 96% and 58% of the BM, respectively.

The use of post-weld heat treatments will be evaluated in the future to assess how the microstructure and properties can be controlled, and eventually improved, after welding.

CRediT authorship contribution statement

J.G. Lopes: Investigation, Data curation, Formal analysis, Writing – original draft. **Priyanka Agrawal:** Investigation, Data curation, Writing – review & editing. **Jiajia Shen:** Investigation. **N. Schell:** Investigation. **Rajiv S. Mishra:** Resources, Investigation, Writing – review & editing. **J. P. Oliveira:** Conceptualization, Resources, Investigation, Data curation, Formal analysis, Project administration, Supervision.

Declaration of competing interest

The authors declare that they have no known competing financial interests or personal relationships that could have appeared to influence the work reported in this paper.

Data availability

Data will be made available on request.

Acknowledgments

JGL, JS and JPO acknowledge Fundação para a Ciência e a Tecnologia (FCT - MCTES) for its financial support via the project UID/00667/2020 (UNIDEMI).

JPO acknowledges the funding by national funds from FCT - Fundação para a Ciência e a Tecnologia, I.P., in the scope of the projects LA/P/0037/2020, UIDP/50025/2020 and UIDB/50025/2020 of the Associate Laboratory Institute of Nanostructures, Nanomodelling and Nanofabrication – i3N.

JGL acknowledges FCT – MCTES for funding the Ph.D. grant 2020.07350. BD.

JS acknowledges the China Scholarship Council for funding the Ph.D. grant (CSC NO. 201808320394).

The raw and processed data required to reproduce these findings cannot be shared as it forms a part of an ongoing study.

The raw/processed data required to reproduce these findings cannot be shared at this time as the data also forms part of an ongoing study.

References

[1] B. Cantor, I.T.H. Chang, P. Knight, A.J.B. Vincent, Microstructural development in equiatomic multicomponent alloys, Mater. Sci. Eng. 375–377 (2004) 213–218, https://doi.org/10.1016/j.msea.2003.10.257.

[2] J.W. Yeh, S.K. Chen, S.J. Lin, J.Y. Gan, T.S. Chin, T.T. Shun, C.H. Tsau, S.Y. Chang, Nanostructured high-entropy alloys with multiple principal elements: novel alloy design concepts and outcomes, Adv. Eng. Mater. 6 (2004) 299–303, https://doi.org/10.1002/ADEM.200300567.

[3] Q. Wu, Y. Jia, Z. Wang, F. He, Y. Wei, J. Li, J. Wang, Rapid alloy design from superior eutectic high-entropy alloys, Scripta Mater. 219 (2022), 114875, https://doi.org/10.1016/J.SCRIPTAMAT.2022.114875.

[4] D.A. Santana, K.R. Santos, C.S. Kiminami, F.G. Coury, Design, phase equilibria, and coarsening kinetics of a new γ/γ′ precipitation-hardened multi-principal element alloy, J. Alloys Compd. 882 (2021), 160729, https://doi.org/10.1016/J.JALLCOM.2021.160729.

[5] H.S. Do, T.J. Jang, K.J. Kim, S.S. Sohn, B.J. Lee, A novel high-entropy alloy with multi-strengthening mechanisms: activation of TRIP effect in C-doped high-entropy alloy, Mater. Sci. Eng. 859 (2022), 144220, https://doi.org/10.1016/J.MSEA.2022.144220.

[6] W. Wang, K. Yang, Q. Wang, P. Dai, H. Fang, F. Wu, Q. Guo, P.K. Liaw, N. Hua, Novel Ti-Zr-Hf-Nb-Fe refractory high-entropy alloys for potential biomedical applications, J. Alloys Compd. 906 (2022), 164383, https://doi.org/10.1016/J.JALLCOM.2022.164383.

[7] L. Cui, Z. Zhang, X.G. Chen, Development of lightweight Al-based entropy alloys for elevated temperature applications, J. Alloys Compd. 938 (2023), 168619, https://doi.org/10.1016/J.JALLCOM.2022.168619.

[8] S. Longfei, H. Wenbin, L. Bokai, W. Shan, K. lei, G. Xingpeng, Corrosion behavior of AlCoCrFeNi2.1 eutectic high-entropy alloy in Cl–containing solution, J. Alloys Compd. 938 (2023), 168609, https://doi.org/10.1016/J.JALLCOM.2022.168609.

[9] C. Zhang, Q. Yu, Y.T. Tang, M. Xu, H. Wang, C. Zhu, J. Ell, S. Zhao, B. E. MacDonald, P. Cao, J.M. Schoenung, K.S. Vecchio, R.C. Reed, R.O. Ritchie, E. J. Lavernia, Strong and ductile FeNiCoAl-based high-entropy alloys for cryogenic to elevated temperature multifunctional applications, Acta Mater. 242 (2023), 118449, https://doi.org/10.1016/J.ACTAMAT.2022.118449.

[10] Z. Li, C.C. Tasan, K.G. Pradeep, D. Raabe, A TRIP-assisted dual-phase high-entropy alloy: grain size and phase fraction effects on deformation behavior, Acta Mater. 131 (2017) 323–335, https://doi.org/10.1016/J.ACTAMAT.2017.03.069.

[11] M.S. Rizi, H. Minouei, B.J. Lee, H. Pouraliakbar, M.R. Toroghinejad, S.I. Hong, Hierarchically activated deformation mechanisms to form ultra-fine grain microstructure in carbon containing FeMnCoCr twinning induced plasticity high entropy alloy, Mater. Sci. Eng. 824 (2021), 141803, https://doi.org/10.1016/J.MSEA.2021.141803.

[12] M.S. Rizi, H. Minouei, B.J. Lee, H. Pouraliakbar, M.R. Toroghinejad, S.I. Hong, Data supporting the hierarchically activated deformation mechanisms to form ultra-fine grain microstructure in carbon containing FeMnCoCr twinning induced plasticity high entropy alloy, Data Brief 42 (2022), 108052, https://doi.org/10.1016/J.DIB.2022.108052.

[13] Y. Hou, Z. Li, L. Chen, Z. Xiang, P. Dai, J. Chen, SLM Fe50Mn30Co10Cr10 metastable high entropy alloy with Al-Ti addition: synergizing strength and ductility, J. Alloys Compd. 941 (2023), 168830, https://doi.org/10.1016/J.JALLCOM.2023.168830.

[14] K. Lu, J. Li, Y. Wang, X. Ma, Excellent strength-ductility synergy and corrosion resistance in a metastable high entropy alloy via heterogeneous structure design, J. Alloys Compd. 941 (2023), 168979, https://doi.org/10.1016/J.JALLCOM.2023.168979.

[15] J. Shen, P. Agrawal, T.A. Rodrigues, J.G. Lopes, N. Schell, J. He, Z. Zeng, R. S. Mishra, J.P. Oliveira, Microstructure evolution and mechanical properties in a gas tungsten arc welded Fe42Mn28Co10Cr15Si5 metastable high entropy alloy, Mater. Sci. Eng. 867 (2023), 144722, https://doi.org/10.1016/J.MSEA.2023.144722.

[16] J.G. Lopes, J.P. Oliveira, A short review on welding and joining of high entropy alloys, Metals 10 (2020) 212, https://doi.org/10.3390/met10020212.

[17] J.P. Oliveira, T.G. Santos, R.M. Miranda, Revisiting fundamental welding concepts to improve additive manufacturing: from theory to practice, Prog. Mater. Sci. 107 (2020), 100590, https://doi.org/10.1016/J.PMATSCI.2019.100590.

[18] Z. Fu, P. Wu, S. Zhu, K. Gan, D. Yan, Z. Li, Effects of interstitial C and N on hydrogen embrittlement behavior of non-equiatomic metastable FeMnCoCr high-entropy alloys, Corrosion Sci. 194 (2022), 109933, https://doi.org/10.1016/J.CORSCI.2021.109933.

[19] J. Ahmed, M. Daly, Yield strength insensitivity in a dual-phase high entropy alloy after prolonged high temperature annealing, Mater. Sci. Eng. 820 (2021), 141586, https://doi.org/10.1016/J.MSEA.2021.141586.

[20] Z. He, N. Jia, H. Yan, Y. Shen, M. Zhu, X. Guan, X. Zhao, S. Jin, G. Sha, Y. Zhu, C. T. Liu, Multi-heterostructure and mechanical properties of N-doped FeMnCoCr high entropy alloy, Int. J. Plast. 139 (2021), 102965, https://doi.org/10.1016/J.IJPLAS.2021.102965.

[21] Z.F. He, N. Jia, D. Ma, H.L. Yan, Z.M. Li, D. Raabe, Joint contribution of transformation and twinning to the high strength-ductility combination of a FeMnCoCr high entropy alloy at cryogenic temperatures, Mater. Sci. Eng. 759 (2019) 437–447, https://doi.org/10.1016/J.MSEA.2019.05.057.

[22] G. Li, M. Liu, S. Lyu, M. Nakatani, R. Zheng, C. Ma, Q. Li, K. Ameyama, Simultaneously enhanced strength and strain hardening capacity in FeMnCoCr high-entropy alloy via harmonic structure design, Scripta Mater. 191 (2021) 196–201, https://doi.org/10.1016/J.SCRIPTAMAT.2020.09.036.

[23] Y. ling Gu, M. ling Yi, Y. Chen, J. Tu, Z. ming Zhou, J. ru Luo, Effect of the amount of SiC particles on the microstructure, mechanical and wear properties of FeMnCoCr high entropy alloy composites, Mater. Char. 193 (2022), 112300, https://doi.org/10.1016/J.MATCHAR.2022.112300.

[24] Z.F. He, N. Jia, H.W. Wang, Y. Liu, D.Y. Li, Y.F. Shen, The effect of strain rate on mechanical properties and microstructure of a metastable FeMnCoCr high entropy

alloy, Mater. Sci. Eng. 776 (2020), 138982, https://doi.org/10.1016/J.MSEA.2020.138982.
[25] F. Yang, L. Dong, X. Hu, X.F. Zhou, F. Fang, Z. Xie, J. Jiang, Microstructural features and tensile behaviors of a novel FeMnCoCr high entropy alloys, Mater. Lett. 275 (2020), 128154, https://doi.org/10.1016/J.MATLET.2020.128154.
[26] J. Kieffer, V. Valls, N. Blanc, C. Hennig, New tools for calibrating diffraction setups, Issn:1600-5775, Urn 27 (2020) 558–566, https://doi.org/10.1107/S1600577520000776.
[27] Y. Liu, J. Tu, L. Deng, C. hao Wang, Z. ming Zhou, Z. tao Jiang, J. ru Luo, Characteristics of thermal- and strain-induced ε-martensite in Fe50Mn30Co10Cr10 multi-component alloy: effect of grain size, Mater. Char. 171 (2021), 110817, https://doi.org/10.1016/J.MATCHAR.2020.110817.
[28] A.M. Hossain, N. Kumar, Microstructure and mechanical properties of a dual phase transformation induced plasticity Fe-Mn-Co-Cr high entropy alloy, J. Alloys Compd. 893 (2022), 162152, https://doi.org/10.1016/J.JALLCOM.2021.162152.
[29] Z. Nishiyama, M.E. Fine, M. Meshii, C.M. Wayman, Martensitic Transformation, Academic Press, 1978.
[30] M. Saboktakin Rizi, H. Minouei, B.J. Lee, M.R. Toroghinejad, S.I. Hong, Effects of carbon and molybdenum on the nanostructural evolution and strength/ductility trade-off in Fe40Mn40Co10Cr10 high-entropy alloys, J. Alloys Compd. 911 (2022), 165108, https://doi.org/10.1016/J.JALLCOM.2022.165108.
[31] Y. Liu, J. Tu, L. Deng, C. hao Wang, Z. ming Zhou, Z. tao Jiang, J. ru Luo, Characteristics of thermal- and strain-induced ε-martensite in Fe50Mn30Co10Cr10 multi-component alloy: effect of grain size, Mater. Char. 171 (2021), 110817, https://doi.org/10.1016/J.MATCHAR.2020.110817.
[32] Z. Li, K.G. Pradeep, Y. Deng, D. Raabe, C.C. Tasan, Metastable high-entropy dual-phase alloys overcome the strength–ductility trade-off, Nature 534 (7606) (2016) 227–230, https://doi.org/10.1038/nature17981, 2016 534.
[33] Z. Li, C.C. Tasan, K.G. Pradeep, D. Raabe, A TRIP-assisted dual-phase high-entropy alloy: grain size and phase fraction effects on deformation behavior, Acta Mater. 131 (2017) 323–335, https://doi.org/10.1016/J.ACTAMAT.2017.03.069.
[34] Y. Liu, J. Tu, L. Deng, C. hao Wang, Z. ming Zhou, Z. tao Jiang, J. ru Luo, Characteristics of thermal- and strain-induced ε-martensite in Fe50Mn30Co10Cr10 multi-component alloy: effect of grain size, Mater. Char. 171 (2021), 110817, https://doi.org/10.1016/J.MATCHAR.2020.110817.
[35] S.I. Wright, M.M. Nowell, D.P. Field, A review of strain analysis using electron backscatter diffraction, Microsc. Microanal. 17 (2011) 316–329, https://doi.org/10.1017/S1431927611000055.
[36] S.S. Rui, Q.N. Han, X. Wang, S. Li, X. Ma, Y. Su, Z. Cai, D. Du, H.J. Shi, Correlations between two EBSD-based metrics Kernel Average Misorientation and Image Quality on indicating dislocations of near-failure low alloy steels induced by tensile and cyclic deformations, Mater. Today Commun. 27 (2021), 102445, https://doi.org/10.1016/J.MTCOMM.2021.102445.
[37] P. Erdely, P. Staron, E. Maawad, N. Schell, H. Clemens, S. Mayer, Lattice and phase strain evolution during tensile loading of an intermetallic, multi-phase γ-TiAl based alloy, Acta Mater. 158 (2018) 193–205, https://doi.org/10.1016/J.ACTAMAT.2018.07.062.
[38] J.P. Oliveira, T.M. Curado, Z. Zeng, J.G. Lopes, E. Rossinyol, J.M. Park, N. Schell, F. M.B. Fernandes, H.S. Kim, Gas tungsten arc welding of as-rolled CrMnFeCoNi high entropy alloy, Mater. Des. 189 (2020), 108505, https://doi.org/10.1016/j.matdes.2020.108505.
[39] J. Shen, J.G. Lopes, Z. Zeng, Y.T. Choi, E. Maawad, N. Schell, H.S. Kim, R.S. Mishra, J.P. Oliveira, Deformation behavior and strengthening effects of an eutectic AlCoCrFeNi2.1 high entropy alloy probed by in-situ synchrotron X-ray diffraction and post-mortem EBSD, Mater. Sci. Eng. 872 (2023), 144946, https://doi.org/10.1016/J.MSEA.2023.144946.
[40] Y. Zhao, J. Zhang, Microstrain and grain-size analysis from diffraction peak width and graphical derivation of high-pressure thermomechanics, Issn:0021-8898, Urn 41 (2008) 1095–1108, https://doi.org/10.1107/S0021889808031762.
[41] B. Bocklund, L.D. Bobbio, R.A. Otis, A.M. Beese, Z.K. Liu, Experimental validation of Scheil–Gulliver simulations for gradient path planning in additively manufactured functionally graded materials, Materialia (Oxf). 11 (2020), 100689, https://doi.org/10.1016/J.MTLA.2020.100689.
[42] A. Röttger, J. Boes, F. Großwendt, S. Weber, Description of a new concept for the development of adapted hot-work tool steels for laser-powder bed fusion, Addit. Manuf. 61 (2023), 103292, https://doi.org/10.1016/J.ADDMA.2022.103292.
[43] M.v. Klimova, D.G. Shaysultanov, S.v. Zherebtsov, N.D. Stepanov, Effect of second phase particles on mechanical properties and grain growth in a CoCrFeMnNi high entropy alloy, Mater. Sci. Eng. 748 (2019) 228–235, https://doi.org/10.1016/J.MSEA.2019.01.112.
[44] A.M. Hossain, N. Kumar, Microstructure and mechanical properties of a dual phase transformation induced plasticity Fe-Mn-Co-Cr high entropy alloy, J. Alloys Compd. 893 (2022), 162152, https://doi.org/10.1016/J.JALLCOM.2021.162152.